Article

A Numerical Method to Determine the Radial Electromagnetic Force of the Switched Reluctance Motor Under Air Gap Eccentricity

Tianji Ma [1,*], **Zhaoxue Deng** [1,2], **Wanli Liu** [3] **and Mengmeng Hou** [1]

[1] School of Mechatronics and Vehicle Engineering, Chongqing Jiaotong University, Chongqing 400074, China; dengzhaoxue@cqjtu.edu.cn (Z.D.); hmmjyo@163.com (M.H.)
[2] Research and Development Department, Changan Automobile Company Ltd., Chongqing 400023, China
[3] China Merchants Testing Vehicle Technology Research Institute Co., Ltd., Chongqing 400050, China; liuwanli1@cmhk.com
[*] Correspondence: lotharpferd@gmail.com; Tel.: +(86)-158-0551-3290

Abstract: This paper discusses a numerical model for determining the radial electromagnetic force of switched reluctance motors under air gap eccentricity (vertical and tilt eccentricities). The authors compare experimental and simulation results to demonstrate that the proposed model can accurately simulate the behavior of radial forces in switched reluctance motors under various types of air gap eccentricity. Moreover, the paper attempts to establish a dynamic model of the SRM and nalyze the performance of the radial electromagnetic force under air gap eccentricity in typical scenarios.

Keywords: air gap eccentricity; imbalanced radial force; numerical method; switched reluctance motor

1. Introduction

Switched reluctance motors (SRMs) have garnered widespread attention from researchers and industries due to their high fault tolerance, low manufacturing costs, and high torque density, particularly in applications such as electric vehicles and household appliances [1–3]. However, during operation, the air gap between the stator and rotor can experience various types of eccentricity due to external loading, leading to electromagnetic force imbalance and degrading the motor's performance [4,5]. Furthermore, the nonlinear characteristics of SRMs complicate the investigation of this issue [6,7].

In recent years, many researchers have proposed valuable methods for modeling the nonlinear characteristics of SRMs and addressing the issue of radial electromagnetic force imbalance. Reference [8] uses different shapes of magnetic flux tubes to describe the air gap between the stator and rotor. It employs the flux ratio criterion to determine the nonlinear permeability of motor materials under different excitation currents, thereby deriving the motor's nonlinear characteristics. References [9–12] have obtained detailed magnetic flux paths in the air gap through comprehensive geometric parameter calculations and used the equivalent magnetic circuit method to determine the permeability at various positions within the gap. Reference [13] introduces variations in the stator–rotor angle into the equivalent magnetic circuit through geometric calculations, enabling the model to analyze the nonlinear variations of motor flux. References [14,15] acquire motor inductance data through finite element sampling and obtain the nonlinear relationship of the flux linkage concerning excitation current and the stator–rotor angle using Fourier series fitting and electromechanical coupling equations. Reference [16] utilizes the Fröhlich–Kennelly equation to interpolate the magnetic flux path at the alignment position of the stator and rotor, resulting in an accurate motor flux linkage model. Reference [17] combines the equivalent magnetic circuit method and curve fitting techniques, employing piecewise polynomial fitting to derive the nonlinear curve of ferromagnetic materials within the

equivalent magnetic circuit. Reference [18] combines magnetic potential with permeability correction to derive the expression for radial electromagnetic force in the air gap through the equivalent magnetic circuit method. Reference [19] builds on the Fourier series fitting of the motor's nonlinear characteristics by adding the virtual displacement principle and stress tensor method to obtain the spatial distribution of radial electromagnetic force at the alignment position. Reference [20] incorporates air gap parameters into the equivalent magnetic circuit method to derive the inductance expression, subsequently using the virtual displacement principle to obtain the radial force expression of the motor. All of these studies have verified the feasibility of the proposed methods through finite element software.

It is evident that the articles mentioned above primarily focus on the establishment of radial force models for SRMs based on their nonlinear characteristics. However, there is a lack of research on the electromagnetic radial force of SRMs under air gap eccentricity, especially regarding the imbalance of radial electromagnetic force due to tilt eccentricity. Therefore, this paper first establishes a radial electromagnetic force model under vertical eccentricity using the principle of virtual displacement and finite element inductance data. Based on this model and the analysis of air gap geometric relationships, a modeling method for the electromagnetic radial force of SRMs under tilt air gap eccentricity is roposed. A dynamic model of the SRMs is established to analyze the radial electromagnetic force in typical dynamic eccentric scenarios.

The remainder of this paper is organized as follows: Section 2 analyzes the types of air gap eccentricity in SRMs. Section 3 proposes a modeling method for the radial force of SRMs under tilt eccentricity based on the research methods for vertical air gap eccentricity. The rest of Section 3 establishes a test bench to validate the accuracy of the proposed modeling method. Section 4 specifies a dynamic motor model based on the electromechanical coupling relationship to analyze the specific manifestations of electromagnetic force imbalance in typical air gap eccentric scenarios.

2. Varieties of Air Gap Eccentricity

The air gap eccentricity in SRMs refers to displacement due to abrupt external excitations, such as load position and magnitude changes. Common types of air gap eccentricity include vertical and tilt eccentricities. When the SRM operates stably, the air gap lengths between the stator and rotor remain consistent in the vertical direction. This results in equal radial electromagnetic forces, F_{r1} and F_{r2}, with no electromagnetic force imbalance, as illustrated in Figure 1a. When vertical eccentricity occurs, with the stator remaining stationary and the rotor translating upward, the upper air gap length decreases. In contrast, the lower air gap length increases, resulting in a differential in radial electromagnetic forces and generating an unbalanced radial electromagnetic force, as shown in Figure 1b. In the case of tilt eccentricity, the stator remains stationary. In contrast, the rotor tilts at an angle, causing changes in the air gap length along the axial direction between the two phases, which alters the radial electromagnetic force at axial positions and produces an unbalanced radial electromagnetic force at axial positions and produces an unbalanced radial torque along the axial direction, as depicted in Figure 1c. These imbalances in radial electromagnetic forces can lead to vibrations and noise during motor operation.
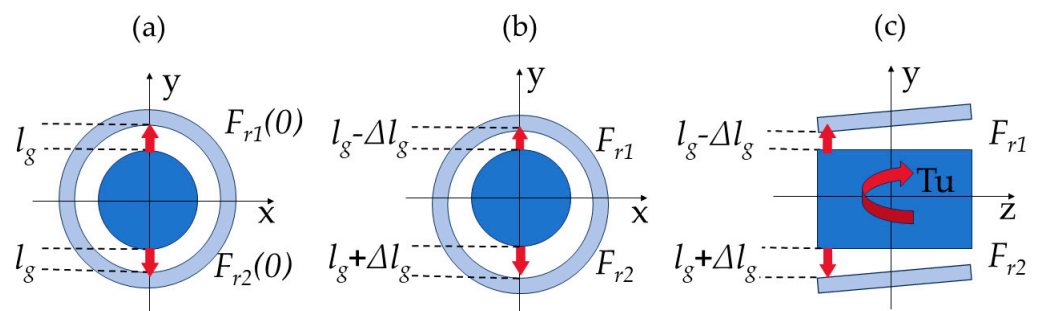

Figure 1. Common air-gap status of SRM: (**a**) no eccentricity, (**b**) vertical eccentricity, (**c**) tilt eccentricity.

This paper uses a four-phase 8/6 pole external rotor switched reluctance motor as the research object, consisting of an external rotor, stator, and winding, as shown in Figure 2. In addition, the structural parameters of the motor are shown in Table 1.
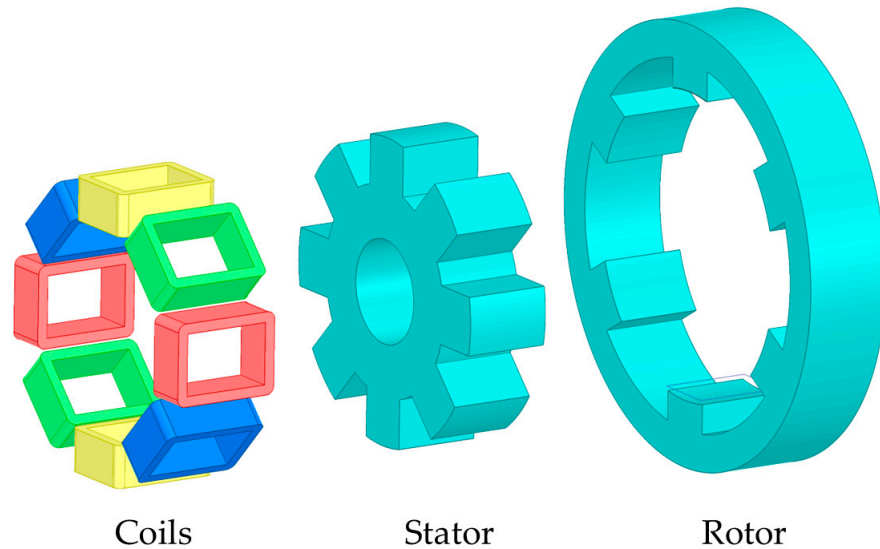

Figure 2. The 8/6 pole external rotor SRM built in Ansys Electronics (2021 R1).

Table 1. Parameters of SRM.

Parameters	Value	Parameters	Value
Rotor Diameter (D_r) [mm]	382	Rotor Pole Arc (β_r) [deg]	23
Stator Diameter (D_s) [mm]	266	Stator Pole Arc (β_s) [deg]	22
Shaft Diameter (D_{sh}) [mm]	90	Rotor Yoke (L_r) [mm]	32
Air gap Length (l_g) [mm]	0.5	Stator Yoke (L_s) [mm]	46
Stack Length (H_g) [mm]	74	Number of Turns (N_c) [−]	136

3. Modelling of Radial Electromagnetic Force Under Air Gap Eccentricity

In this section, the expression for radial electromagnetic force in switched reluctance motors under vertical eccentricity is derived in Section 3.1. Then, Section 3.2 analyzes the geometric relationships of the air gap length for tilt eccentricity, and by combining this with the expression for vertical eccentric radial force, the expressions for radial electromagnetic force and unbalanced radial torque under tilt eccentricity are obtained. Finally, Section 3.3 validates the accuracy of the proposed model through experiments and finite element simulations.

3.1. Radial Electromagnetic Force Under Vertical Eccentricity

Firstly, the magnetic co-energy W_m of the switched reluctance motor windings can be expressed as the integral of the winding flux linkage concerning the phase current *i*, as shown in the following equation:

$$W_m = \int_0^i \psi(\theta, i)di \tag{1}$$

where $\Psi(\theta, i)$ is the flux linkage under different rotor rotating positions and phase currents.

According to the principle of virtual displacement, displacement of the current-carrying circuit results in a change in magnetic co-energy. The SRM has displacements in two directions: circumferential angular and radial displacement, corresponding to the motor's static magnetic torque and radial electromagnetic force, respectively. Therefore, the switched reluctance motor's static magnetic torque and radial electromagnetic force

can be represented as the partial derivatives of the magnetic co-energy concerning the rotor angular position and radial displacement under constant current excitation, as shown in the following equation:

$$\begin{cases} T_m = \frac{\partial W_m}{\partial \theta}\Big|i = const = \int_0^i \frac{\partial \psi(\theta,i)}{\partial \theta}di \\ F_r = \frac{\partial W_m}{\partial d_r}\Big|i = const = \int_0^i \frac{\partial \psi(\theta,i)}{\partial d_r}di \end{cases} \tag{2}$$

where T_m is static magnetic torque, F_r is the radial electromagnetic force, θ is the rotor's rotating angle position, i is phase current which is a constant value, and d_r is the air gap length between the stator and rotor.

Since the current i is a constant value, the magnetic flux linkage can be expressed as a single-variable function of the rotor angular position θ. Furthermore, the magnetic flux linkage can also be represented as the integral of the inductance concerning the winding current, indicating that the inductance is likewise a single-variable function of the rotor angular position θ, as shown in the following equation:

$$\psi(\theta,i) = \int_0^i L(\theta,i)di \tag{3}$$

Combing Equations (1)–(3), the radial electromagnetic force expression is as follows:

$$F_r = \frac{1}{2}\frac{L(\theta,i)}{d_r} \cdot i^2 \tag{4}$$

When vertical eccentricity occurs, the air gap length can be expressed as follows:

$$d_r = l_g - \Delta l_g \tag{5}$$

where l_g is the original air gap length and Δl_g is the vertical eccentricity displacement, so Equation (4) can be rewritten as follows:

$$F_r = \frac{1}{2}\frac{L(\theta,i)}{l_g - \Delta l_g} \cdot i^2 \tag{6}$$

In this formula, the vertical eccentricity displacement Δl_g can be expressed as follows:

$$\Delta l_g = \frac{\varepsilon \cdot l_g}{100\%} \tag{7}$$

In this formula, ε is the vertical eccentricity rate, and its value range is 0–100%.

Due to the solid nonlinear characteristics of the winding inductance $L(\theta, i)$ in SRM, the inductance varies under different eccentric conditions. Therefore, the finite element analysis software Ansys Electronics can conveniently obtain data on inductance $L(\theta, i, \varepsilon)$ under varying air gap eccentricities, currents, and rotor positions, as illustrated in Figure 3a. Consequently, based on Equations (6) and (7), the radial electromagnetic force of the switched reluctance motor can be expressed as follows:

$$F_r = \frac{1}{2}\frac{L(\theta,i,\varepsilon)}{(1-\varepsilon)l_g}i^2 \tag{8}$$

Further, Equation (8) provides data on radial electromagnetic force under different vertical air gap eccentricities, currents, and rotor positions, as shown in Figure 3b. The overlap area between the stator and rotor tooth surfaces is maximized at the aligned position (i.e., at half of the mechanical cycle). Therefore, the inductance is most affected by vertical air gap eccentricity at the aligned position, which leads to a significant imbalance in the radial electromagnetic force at this position.
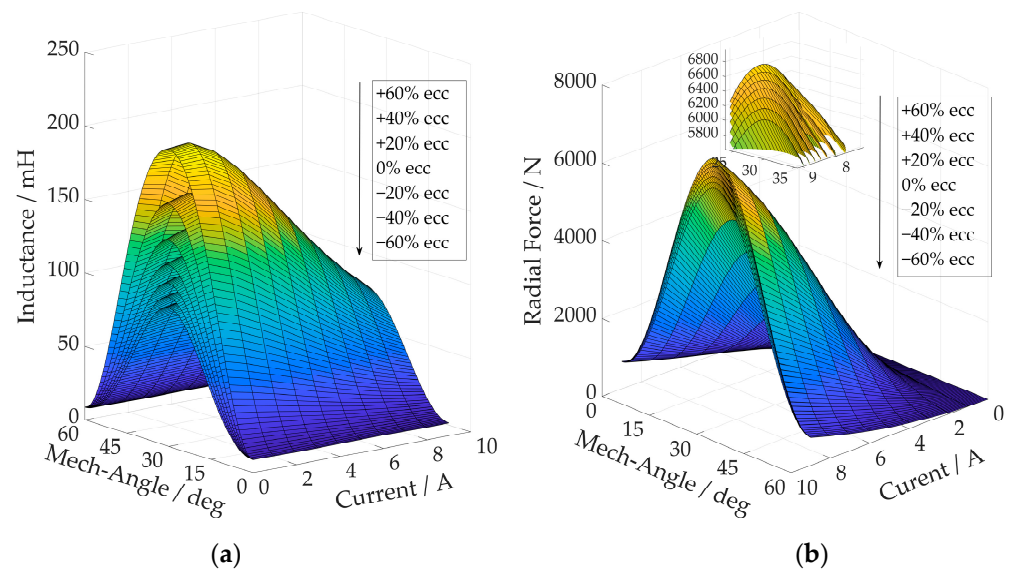
Figure 3. Inductance under vertical eccentricity (**a**) and radial force under vertical eccentricity (**b**).

In a switched reluctance motor, the position of the rotor poles relative to the energized stator poles can be represented by two specific positions: complete misalignment position and alignment position. When the rotor poles are in a state of complete misalignment, the rotor poles are directly opposite the stator yoke, resulting in the maximum air gap and minimum inductance, and consequently, the minimum radial force, corresponding to the 0° mechanical angle position shown in Figure 3a. As the rotor rotates, the air gap length gradually decreases to the length of the air gap between the stator and rotor, which remains constant; however, the overlapping area of the stator and rotor poles increases, leading to an increase in inductance and, subsequently, radial force. When the rotor and stator teeth are completely aligned, the inductance reaches its peak value, and the radial force reaches its maximum, corresponding to the 30° mechanical angle position in Figure 3b. After the rotor crosses the completely aligned position, the overlapping area of the stator and rotor teeth decreases, causing a reduction in inductance and a corresponding decrease in the radial force until it reaches zero. This explains the symmetrical distribution of the inductance and radial force curves about the alignment position shown in Figure 3.

The definitions of positive and negative air gap eccentricity in Figure 3 are as follows: A reduction in air gap length is designated as positive eccentricity, as it results in higher inductance and radial electromagnetic force compared to the scenario without air gap eccentricity. Conversely, increased air gap length is designated as negative eccentricity, leading to lower inductance and radial electromagnetic force than the scenario without air gap eccentricity.

3.2. Radial Force Under Tilt Eccentricity

To analyze the radial electromagnetic force in an SRM under tilt eccentricity, it is first necessary to derive the analytical expression for the air gap length at different axial positions. A schematic diagram of the air gap length at various axial positions without initial eccentricity is shown in Figure 4, where the air gap length is equal at all axial positions.

Set the distance from the rotor's rotation point under tilt air gap eccentricity to the left endpoint of the stator, denoted as l_r, while the air gap length remains the initial length l_g. When one end of the rotor makes contact with the stator, the angle of tilt eccentricity at this point is defined as the maximum tilt eccentricity α_{tmax}. The geometric relationship is illustrated in Figure 4b; thus, the maximum tilt eccentricity angle can be expressed as follows:

$$\alpha_{t\max} \arctan \left(\frac{l_g}{l_r}\right) \tag{9}$$

Since the rotor tilt air gap eccentricity angle can only change between $[0–\alpha_{tmax}.]$, set the tilt eccentricity rate to $\eta\%$, and then the tilt eccentricity angle α_t can be expressed as follows:

$$\alpha_t = \alpha_{tmax} \cdot \eta \tag{10}$$

Therefore, under the specific tilt eccentricity of the air gap, the minimum air gap length l_{gmin} shown in Figure 4c can be expressed as follows:
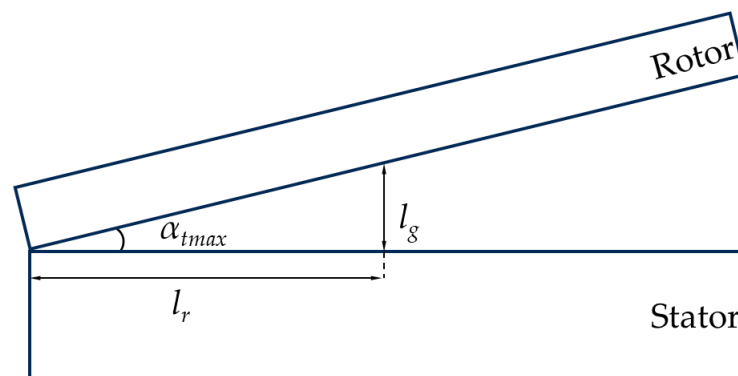
$$l_{gmin} = l_r \cdot \tan(\alpha_t) \tag{11}$$

Further, set the distance from any observation point l_x between the stator's two ends and the stator's left end to be defined. The increment Δl_{gmin} at different observation points, relative to the minimum air gap length is shown in Figure 4d, can be expressed as follows:
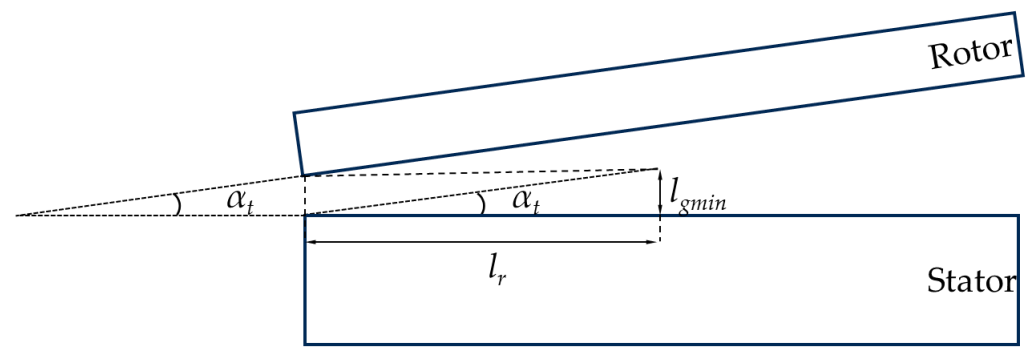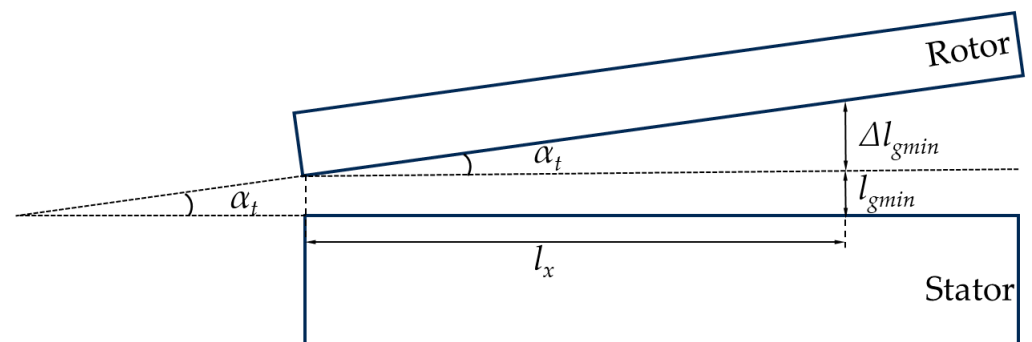
$$\Delta l_{gmin} = l_x \cdot tan(\alpha_t) \tag{12}$$
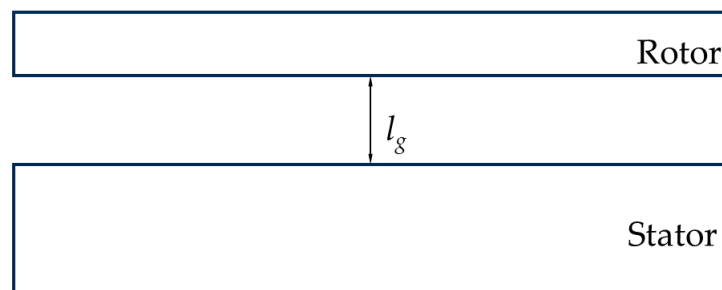
(**a**)

(**b**)

Figure 4. *Cont.*

(c)

(d)

Figure 4. Analysis process of air gap geometric relationship under tilt eccentricity. (**a**) No tilt eccentricity; (**b**) max tilt eccentricity angle; (**c**) minimum air gap length under a specific tilt angle; (**d**) increment of minimum air gap length in axial observation point position.

Combining the above expressions, the final equation for the distribution of air gap length along the axial length of the motor under tilt air gap eccentricity can be obtained as follows:

$$l_{gt}(l_x, \eta, l_r) = l_g - l_r \cdot \tan(\alpha_{t\max} \cdot \eta) + l_x \cdot \tan(\alpha_{t\max} \cdot \eta) \tag{13}$$

where l_g is the original air gap length, l_x is the distance between the observation point and the left side of the stator, η is the tilt eccentricity rate, l_r is the distance between the rotor rotating point and the left side of the stator, and $\alpha_{t\max}$ is the maximum tilt eccentricity degree.

Figure 5 shows the air gap length diagram of different axial lengths and tilt air gap eccentricity rates when l_r is the middle point of the motor's axial length.
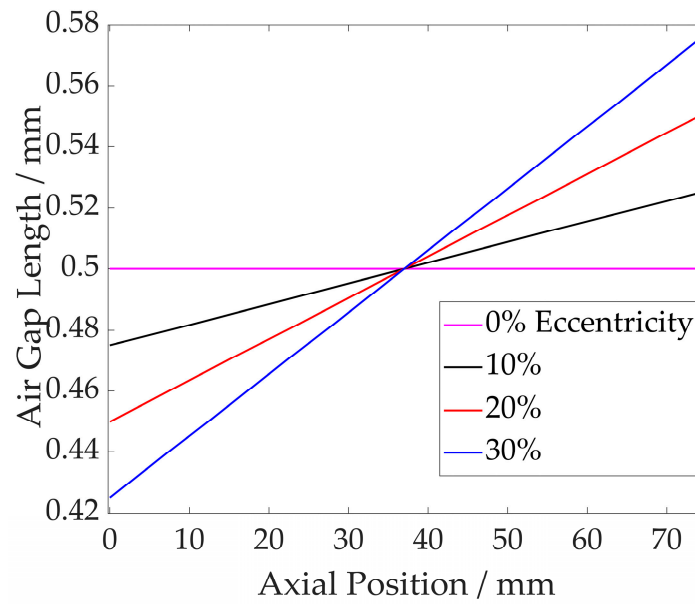
Figure 5. Air gap length under different tilt eccentricity rates η and axial distances l_x.

To simplify the calculation process of tilt eccentricity, the first-order polynomial is used to fit the air gap length under different degrees of eccentricity:

$$L_{airgap} = A_{[n \times 1]} \cdot l_x + B_{[n \times 1]} \tag{14}$$

where A and B represent the air gap length's fitting coefficient and constant term under n skew eccentricities, respectively.

The analytical expression for the radial force under vertical air gap eccentricity can be obtained in (10) by combining it with the expression for the air gap length under tilt eccentricity described above.

$$F_t = \frac{1}{2} \frac{L(\theta, i, \varepsilon)}{A \cdot l_x + B} \cdot i^2 \tag{15}$$

Additionally, the graphs depicting the unbalanced radial force at various degrees of tilt eccentricity rate along the axial position are shown in Figure 6 below.
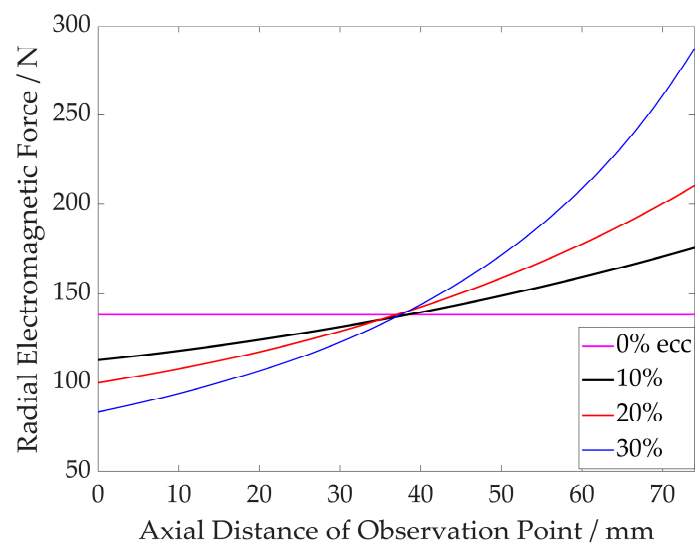

Figure 6. Radial electromagnetic force under different tilt eccentricity rates η and axial distances l_x.

Finally, the expression of the unbalanced radial moment under tilt eccentricity is obtained:

$$T_u = \int_{l_r}^{l_a} F_t dl_x - \int_0^{l_r} F_t dl_x \tag{16}$$

where l_a is the axial length of SRM, and l_r is the rotational point of the rotor under tilt eccentricity.

3.3. Experiment and Finite Element Simulation Verification

A test bench was constructed to validate the proposed modeling method for radial electromagnetic forces in switched reluctance motor SRMs under different eccentric conditions, as shown in Figures 7 and 8. The test bench components were fabricated according to the experimental procedure, including the platform chassis, rotor holder, stator holder, sensor holder, support shaft, and switched reluctance motor. This completed the preliminary assembly of the test setup. Furthermore, the measurement equipment for the radial electromagnetic force of the switched reluctance motor included a multi-channel DC-regulated power supply, tension and pressure sensors, a weight display controller, sensor pressure contact points, a digital multimeter, DCC power test leads, high-precision feeler gauges, and a laptop computer.
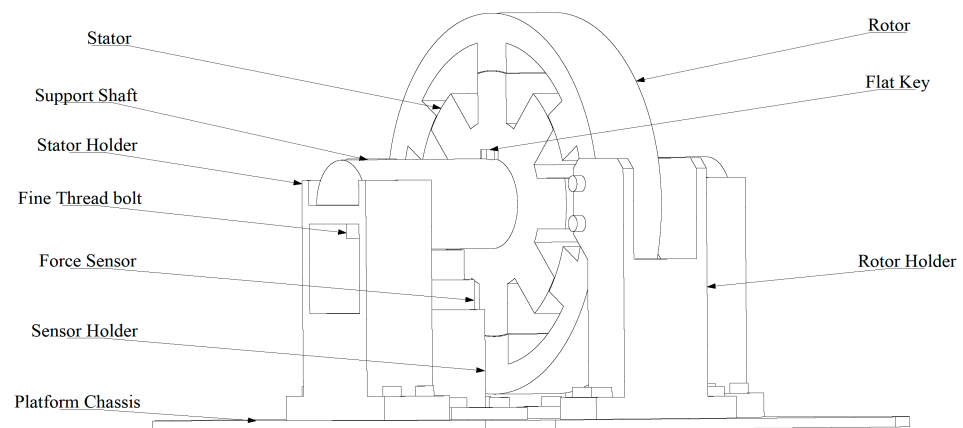

Figure 7. Structure diagram of radial electromagnetic force verification test bench.
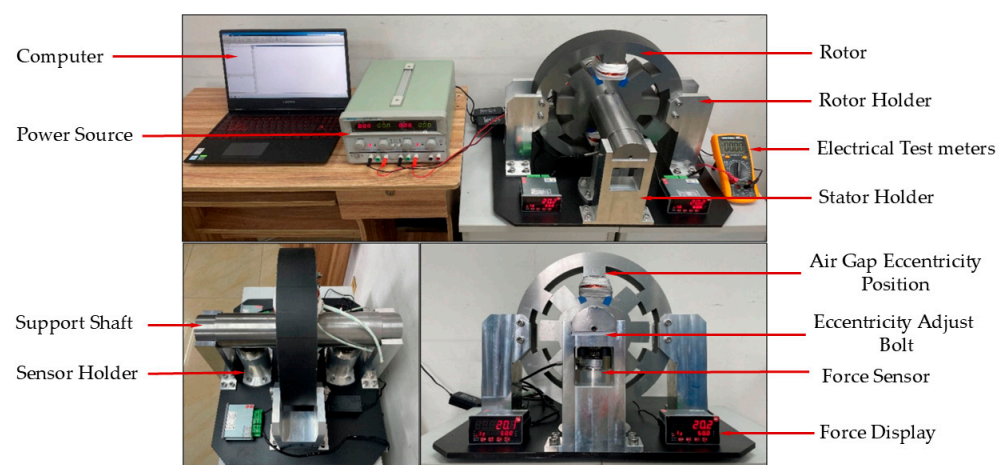

Figure 8. Radial electromagnetic force verification test bench.

The experiment method is as follows: The rotor is connected to the rotor holder by bolts, maintaining a constant vertical height during measurement. The stator is connected to the support shaft via a key, with the support shaft resting on the stator holder and a balancing cushion placed between them to ensure single-degree-of-freedom motion in both

horizontal and vertical directions. A force sensor is equipped with a pressure contact point and mounted on a sensor holder. The size of the air gap eccentricity is adjusted using an adjusting bolt connected to the stator holder, converting the circumferential rotation of the bolt into linear motion in the vertical direction to modify the air gap eccentricity.

During the measurement process, the air gap length is first adjusted to the target value using the adjusting bolt to achieve different types of air gap eccentricity in the switched reluctance motor while also changing the height of the sensor's pressure contact point, ensuring it is free from external forces except for gravity concerning the support shaft. Subsequently, the adjusting bolt is retracted by a certain distance to ensure its tail does not contact the support shaft throughout the measurement process. The radial electromagnetic force under air gap eccentricity is then measured by adjusting the magnitude of the current excitation. Finally, the pressure values obtained from the pressure sensor are recorded in real-time on a laptop, completing the measurement of the radial electromagnetic force and unbalanced radial force under air gap eccentricity in the switched reluctance motor.

Furthermore, since there is no bearing support between the stator and rotor in the test bench when the radial electromagnetic force of the SRM exceeds the weight supported by the stator, winding, and support shaft, the stator and rotor poles may come into contact due to the attractive effect of the radial electromagnetic force. After multiple trials and validations, the measurement threshold of the radial electromagnetic force measurement bench designed in this study is 300 N. In measuring the radial electromagnetic force, this threshold should be fully considered to ensure the measurement process's safety and the measurement results' accuracy.

Based on the experimental method and the test bench, the radial electromagnetic force measurements of SRM were obtained under different levels of vertical air gap eccentricity and winding currents, as shown in Figure 9. The measured radial electromagnetic forces align well with the results derived from the proposed analytical modeling method, effectively validating the accuracy of the proposed method for calculating the radial electromagnetic force under vertical eccentricity.
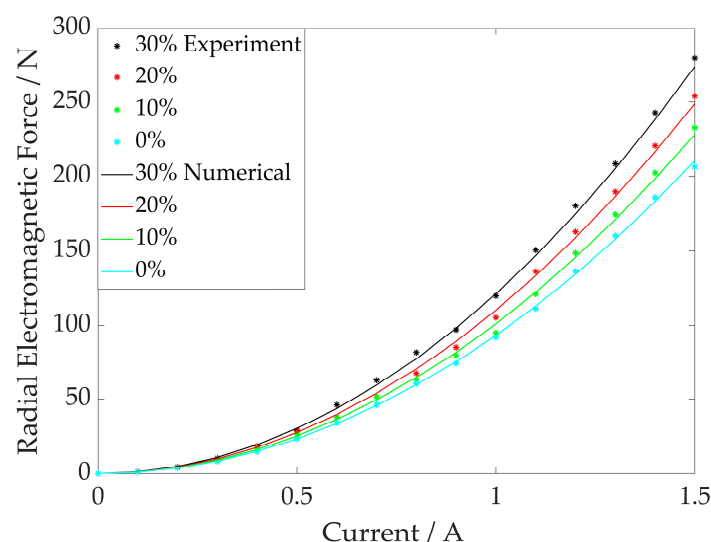

Figure 9. Comparison between the experimental and proposed method's results.

When the switched reluctance motor windings are under a constant current excitation of 1 A, Figure 10a,b show the experimental measurements, finite element simulation results, and analytical results of the proposed modeling method for radial electromagnetic force under various degrees of tilt air gap eccentricity. The experimental, simulation, and numerical model data are summarized in Table 2.
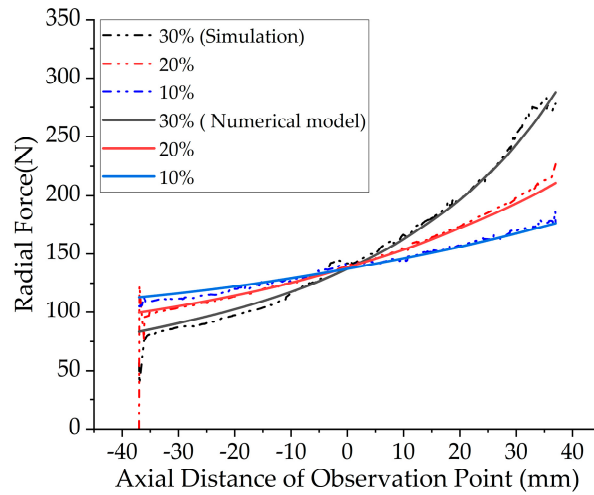
(**a**)
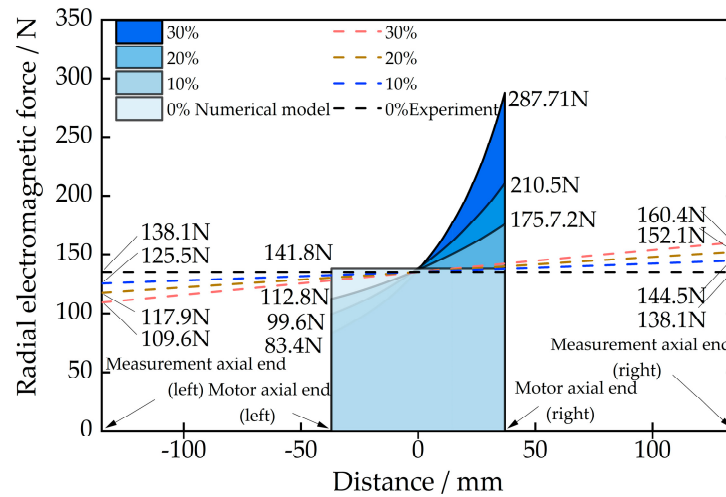
(**b**)

Figure 10. Simulation's result, experiment, and numerical model of radial force under tilt eccentricity. (**a**) Result comparison between simulation and numerical model; (**b**) result comparison between experiment and numerical model.

Table 2. Unbalanced torque between experiment, simulation, and analytical model.

Tilt Eccentricity Rate [%]	Measurement Value [N]		Unbalanced Tilt Torque [Nm]		
	Left Sensor	**Right Sensor**	**Experiment**	**Simulation**	**Numerical Model**
0%	138.1	138.1	0	0	0
10%	125.5	144.5	1.283	1.067	1.166
20%	117.9	152.1	2.309	2.245	2.105
30%	109.6	160.4	3.429	3.724	3.573

Figure 10 and Table 2 show that the proposed tilt eccentric radial electromagnetic force model is highly accurate.

4. Model for Dynamic Air Gap Eccentricity of SRM

In this section, Section 4.1 presents the dynamic model framework for switched reluctance motors and explains the working principles of each module. Then, in Section 4.2, the proposed dynamic model is validated using the motor structure and experimental data provided in the literature. Finally, Section 4.3 investigates the behavior of air gap length and unbalanced radial force/torque in switched reluctance motors under typical dynamic eccentricity scenarios.

4.1. Dynamic Model for SRM

To analyze the radial force performance of switched reluctance motor under dynamic eccentricity, it is necessary to establish the dynamic model of the SRM. The structure of the dynamic model of the SRM is shown in Figure 11.
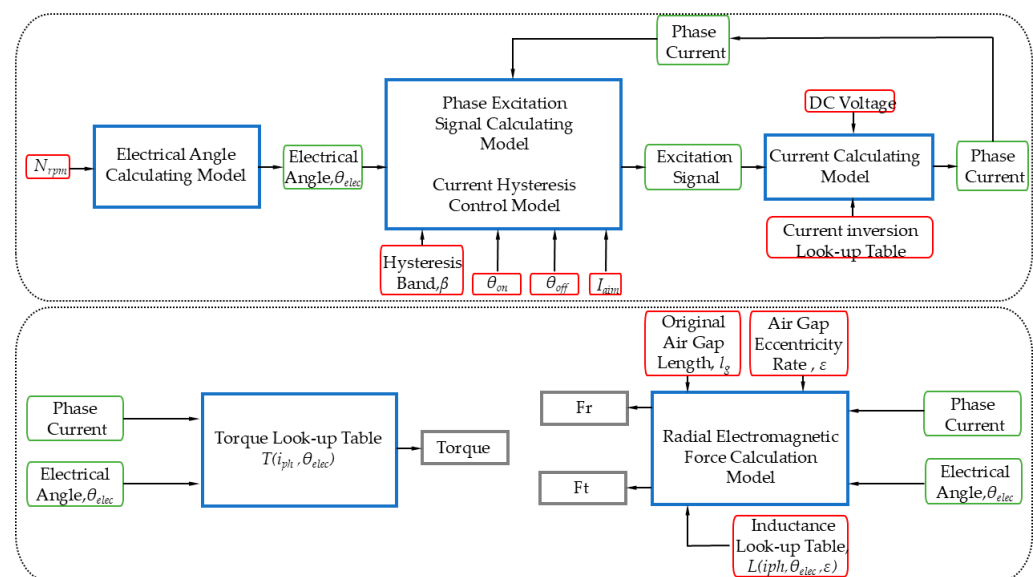

Figure 11. Structure of SRM dynamic model.

The parameters enclosed in the red boxes represent input parameters, those in the blue boxes represent functional modules, the green boxes denote intermediate variables, and the gray boxes indicate output parameters.

Next, the working principles of each module will be described.

4.1.1. Electrical Angle Calculating Module

The rotor electrical angle θ_{elec} can be obtained by calculating the rotor mechanical angle θ_{mech}. Since the rotor position increases linearly at a constant speed, every 360° represents one complete electrical cycle. The mechanical position of the rotor can be calculated using the discrete integration of the rotor's angular velocity, as shown in the following equation:

$$\theta_{mech}(k) = \text{mod}\left(N_{rpm}\left(\frac{360}{60}\right)T_s \cdot k + \theta_{mech0}, 360\right) \quad (17)$$

where N_{rpm} represents the mechanical rotational speed of the motor in RPM; T_s is the sampling time step, i.e., the sampling interval; k represents the kth sampling instance; θ_{mech0} is the initial position of the rotor, which corresponds to the alignment of the first rotor tooth with the first stator pole, and T_s is the sampling time step.

Since the motor has N_r rotor teeth, each electrical cycle consists of N_r repetitions, with the starting electrical angle position defined as the misalignment between the first stator tooth and rotor tooth. Consequently, the alignment position of the stator and rotor

corresponds to an electrical angle of 180°. Therefore, the rotor mechanical angle and electrical angle can be expressed as follows:

$$\theta_{elec} = Nr \cdot \theta_{mech} + 180 \tag{18}$$

Therefore, when the first phase begins to be excited, the electrical angle displacements of the remaining phases can be expressed as follows:

$$\Delta\theta_{elec} = \frac{360}{m} k_{ph} \tag{19}$$

where k_{ph} represents the excitation sequence of the motor phase windings and m denotes the number of phases. Since the subject of this study is a four-phase motor, k_{ph} = [0–3].

Therefore, the expression θ_{elec} is obtained by combining Expressions (17)–(19), and the electrical angle of the motor at a specific speed can be obtained:

$$\theta_{elec}(k) = \mod((N_r \cdot \theta_{mech}(k) + 180) + \frac{360}{m} k_{ph}, 360) \tag{20}$$

where $\theta_{elec}(k)$ is the electrical angle of the rotor at the kth sampling.

4.1.2. Current Calculation Module

The core part of the current calculation model is the formula for the stator winding voltage of the switched reluctance motor:

$$V_{ph} = R_{ph}i_{ph} + \frac{d\lambda_{ph}\left(i_{ph}, \theta_{elec}\right)}{dt} \tag{21}$$

where V_{ph} is phase voltage, R_{ph} is phase reluctance, i_{ph} is phase current, λ_{ph} is phase flux linkage, and θ_{elec} is the rotor's rotation electrical angle.

Further, the integral method can be used to process Equation (12), and the flux linkage data $\lambda_{ph}(t)$ can be obtained:

$$\lambda_{ph}(t) = \int \left(V_{ph}(t) - R_{ph} \cdot i_{ph}(t)\right)dt \tag{22}$$

Due to the high correlation between the phase current i_{ph}, magnetic flux linkage λ_{ph}, and rotor electrical angle position θ_{elec}, the above expression can be rewritten as:

$$\lambda_{ph}(t) = \int \left[V_{ph}(t) - R_{ph} \cdot i_{lut}\left(\lambda_{ph}(t), \theta_{elec}(t)\right)\right]dt \tag{23}$$

In this equation, $i_{lut}(\lambda_{ph}, \theta_{elec})$ represents the current–flux linkage–rotor electrical angle lookup table. Therefore, obtaining the magnetic flux linkage value at a given moment can determine the corresponding current value. Subsequently, using the discrete form of the above expression, the magnetic flux linkage value at the next moment can be calculated as follows:

$$\lambda_{ph}(k+1) = \lambda_{ph}(k) + \left[V_{ph}(k+1) - R_{ph} \cdot i_{lut}\left(\lambda_p(kt), \theta_{elec}(k)\right)\right] \cdot T_s \tag{24}$$

where k is the k-th sampling frequency, $i_{Lut}(\lambda_{ph}(k), \theta_{elec}(k))$ can be obtained through the reverse lookup table of $\lambda_{ph}(i_{ph}(k), \theta_{elec}(k))$, and *Ts* is the sampling time step. The reverse lookup process is illustrated in Figure 12.
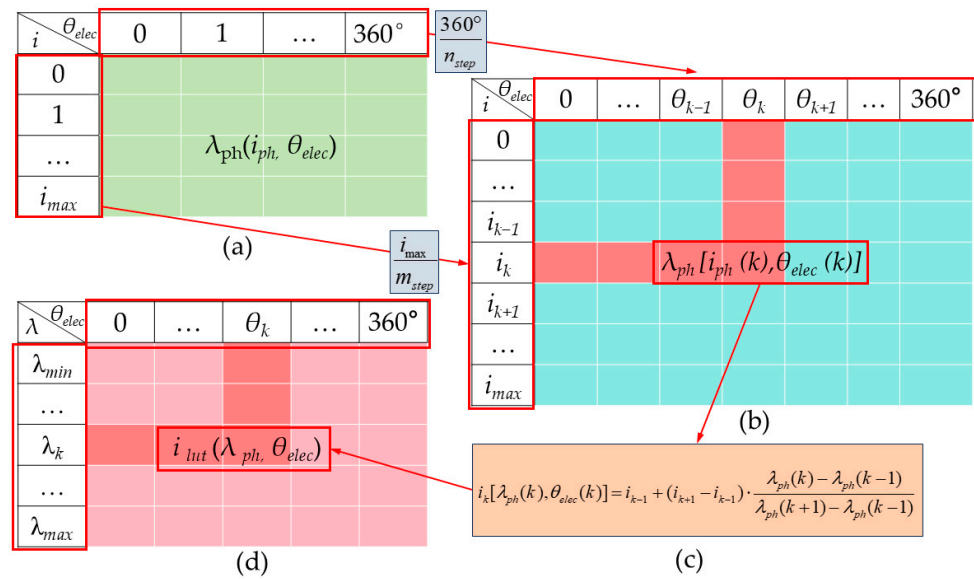
Figure 12. Inverse progress from flux linkage $\lambda_{ph}(i_{ph}(k), \theta_{elec}(k))$ to current $i_{Lut}(\lambda_{ph}(k), \theta_{elec}(k))$.

Figure 12a shows the origin data structure of flux linkage λ which can be obtained by finite element software. First, the number of the rotor electrical angle and phase current are extended to $360/n_{step}$ and I_{max}/m_{step}, respectively. By applying linear interpolation methods, more accurate and comprehensive flux linkage data can be obtained, as shown in Figure 12b. As long as the step size is sufficiently small, precise flux linkage data can be achieved. Then, the flux linkage $\lambda[i_{ph}(k), \theta_{elec}(k)]$ is inverted by the equation, as shown in Figure 12c, to retrieve the lookup table data for the current, $i_{Lut}[\lambda_{ph}(k-1), \theta_{elec}(k-1)]$. Finally, the inversion data structure of current is shown in the Figure 12d.

Figure 13a presents the discrete original flux linkage data $\lambda_{ph}(i_{ph}, \theta_{elec})$ obtained through finite element software. In contrast, Figure 13b shows the current data obtained after executing the inversion process outlined in Figure 12.
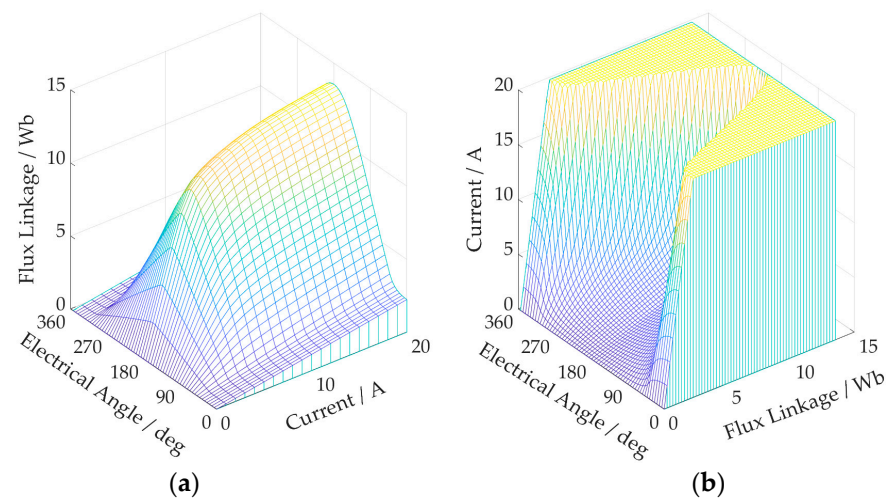

Figure 13. (**a**) Flux linkage $\lambda_{ph}(i_{ph}, \theta_{elec})$; (**b**) inversion current result $i_{Lut}(\lambda_{ph}, \theta_{elec})$.

4.1.3. Current Hysteresis Control Module

Current hysteresis control [21–23] is widely used in the drive systems of switched reluctance motors, primarily for current tracking. The principle is as follows: The motor's phase current is maintained within a reasonable range by setting upper and lower limits for

the current. This is primarily controlled using the upper current limit I_{upper} and the lower current limit I_{lower}, as expressed in the following equation:

$$\begin{cases} I_{upper} = I_{aim} \cdot (1 + \beta) \\ I_{lower} = I_{aim} \cdot (1 - \beta) \end{cases} \tag{25}$$

In the equation, I_{aim} represents the target current and β is the percentage of the current hysteresis bandwidth relative to the target current, typically set at 2% to 5%.

The excitation signal for the winding of the switched reluctance motor can be expressed as follows:

$$Exc(k) = \begin{cases} -1 & \left| \theta_{elec}(k) \geq \theta_{off} \cap i_{ph} > 0 \right. \\ 0 & \left| \theta_{on} \leq \theta_{elec}(k) \leq \theta_{off} \cap i_{ph} > i_{upper} \right. \\ 1 & \left| \theta_{on} \leq \theta_{elec}(k) \leq \theta_{off} \cap i_{ph} < i_{upper} \right. \\ Exc(k-1) & \left| \theta_{on} \leq \theta_{elec}(k) \leq \theta_{off} \cap i_{lower} \leq i_{ph} < i_{upper} \right. \end{cases} \tag{26}$$

In the equation, $Exc(k)$ denotes the excitation signal for the phase winding at the k-th sampling instance, where the symbol $\cap$ indicates 'and', i.e., that both conditions must be simultaneously satisfied.

Thus, based on Equations (25) and (26), real-time plots of phase current and excitation signal can be obtained at specific switching angles, target currents, and current hysteresis bandwidths, as shown in Figure 14.
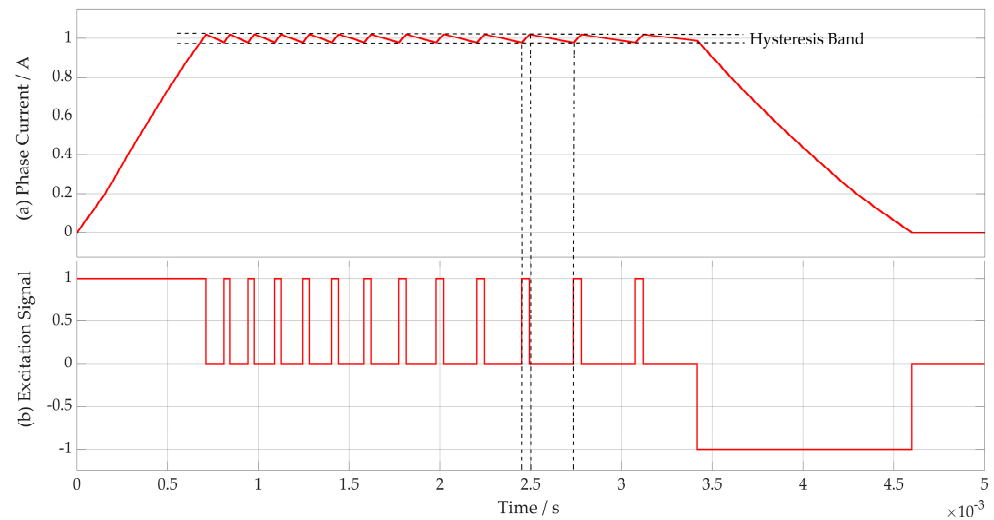

Figure 14. Hysteresis Control: (**a**) phase current waveform; (**b**) phase voltage waveform.

From the figure, the real-time phase current fluctuates within the hysteresis band. When the rotor angle exceeds the turn-on angle, and the phase current is less than the target current, the excitation signal is set to 1, indicating that the circuit is conducting in the forward direction. Conversely, when the phase current is greater than or equal to the upper limit I_{upper}, the excitation signal is set to 0, indicating that the circuit is off and the current decreases gradually. When the current drops to or below the lower limit I_{lower}, the excitation signal returns to 1, indicating that the circuit is again conducting forward. This cycle continues until the rotor angle passes the turn-off angle, at which point the excitation signal changes to −1, indicating reverse conduction of the circuit, causing the phase current to drop rapidly to zero. Finally, the excitation signal remains at 0, fully disconnecting the phase winding until the rotor angle again passes the turn-on angle.

4.1.4. Torque and Radial Force Calculation Module

The torque module is centered around the static torque lookup table $T_{lut}(i_{ph}, \theta_{elec})$, with phase current i_{ph} and rotor electrical angle θ_{elec} inputs; it produces real-time torque T as output. This torque lookup table can be obtained by solving the electromechanical energy conversion and virtual displacement equations or through finite element simulations.

The radial force calculation module is based on the expressions for radial electromagnetic force under vertical and tilt eccentricities proposed in Section 3. Its inputs include the initial air gap eccentricity l_g, the rate of change of air gap eccentricity ε, and the inductance under air gap eccentricity $L(i_{ph}, \theta_{elec}, \varepsilon)$. The outputs consist of the unbalanced radial force under vertical eccentricity and the unbalanced radial torque under tilt eccentricity.

The dynamic model of the switched reluctance motor, centered on the electrical angle calculation module and real-time current module, has been successfully established.

4.2. Dynamic Model Verification

To validate that the proposed model can correctly compute phase current and electrical angle, as well as ensure a certain level of simulation accuracy, this section employs two switched reluctance motor models from reference [20] for verification, with motor structural parameters, excitation parameters, operating conditions, and output parameters all sourced from reference [20].

First, based on the switched reluctance motor parameters provided in reference [20], the motors are modeled using finite element software, as shown in Figure 15. This process further yields flux and torque data for different currents and rotor angles. Next, the current–angle–flux inversion process in Figure 13 is performed, resulting in a lookup table for flux–angle–real-time current. Subsequently, this real-time current table and torque table are input into the proposed dynamic model of the switched reluctance motor. Finally, based on the motor output parameters and data obtained from reference [20], a comparison of results is shown in Table 3.

The specific operating conditions for model validation are 200 turns of winding coils, an excitation current of 6A, and a target speed of 200 RPM. The control method used is chopped current control (CCC). Table 3 compares the motor's output parameters.

Table 3 shows that under consistent input and output parameters, the output parameters computed by the proposed dynamic simulation model match the experimental data provided in reference [20]. This proves the accuracy of the proposed dynamic model for the SRM.
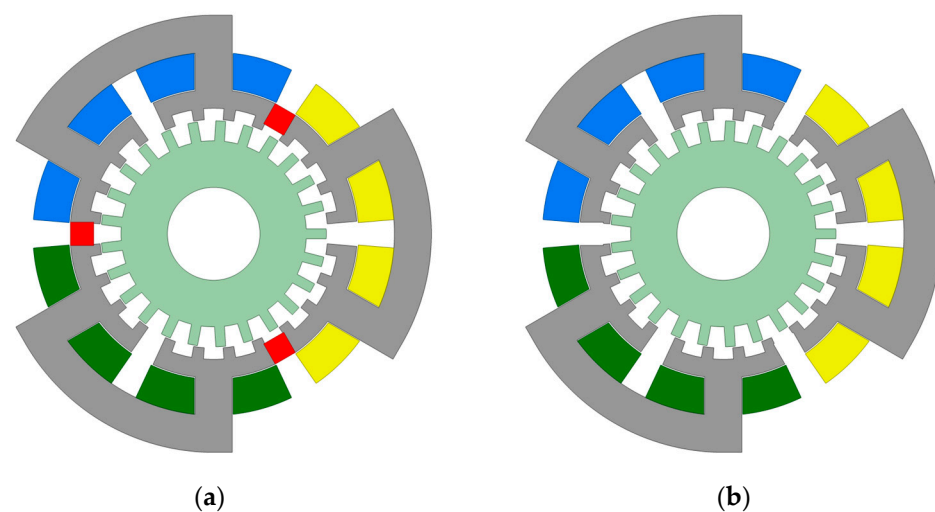

(**a**)   (**b**)

Figure 15. Verification SRM from reference [20]. (**a**) MTPMSRM [20]; (**b**) MTSRM [20].

Table 3. Result of the dynamic model and the experiment reference [20].

Output Parameters		MTSRM [22] Experiment	Proposed Dynamic Model	Error, %	MTPMSRM [22] Experiment	Proposed Dynamic Model	Error, %
Static Torque Performance	Current [A]	6	6	-	6	6	-
	Maximum Torque [Nm]	0.85	0.831	2.286	1.43	1.449	1.328
	Average Torque [Nm]	0.54	0.524	3.053	0.86	0.875	1.744
Dynamic Torque Performance	Rotation Speed [RPM]	200	200	-	200	200	-
	RMS Current [A]	3.05	3.061	0.361	2.37	2.384	0.415
	Maximum Torque [Nm]	0.85	0.851	0.117	1.43	1.434	0.279
	Average Torque [Nm]	0.41	0.442	7.805	0.67	0.695	8.209
	Torque Ripple [%]	121	124	2.479	119	123	3.361
	Torque per Ampere [Nm/A]	0.13	0.139	6.923	0.28	0.302	7.857

The parameters in Table 3 are explained as follows: Maximum torque can be defined in two ways: the maximum value of static torque under constant winding excitation and the maximum value of dynamic torque under constant winding excitation and speed. The average torque is defined similarly. The RMS current refers to the root mean square value of the dynamic current, also known as the effective current. Torque ripple is defined as the difference between the maximum and minimum torque expressed as a percentage of the average torque, commonly used to assess the stability of the motor's output torque [24]. Torque per ampere refers to the average torque that the motor can output for each ampere of current and is often used to evaluate the torque density of the motor [25].

4.3. Dynamic Eccentricity Analysis

This section selects typical scenarios of dynamic vertical and tilt air gap eccentricity in switched reluctance motors and analyzes the performance of radial electromagnetic force in these scenarios.

Taking the switched reluctance hub-driven motor as an example, since this type of drive motor's hub is directly connected to the outer rotor, various external excitations will directly affect the hub and outer rotor, resulting in dynamic air gap eccentricity.

When the switched reluctance hub-driven motor is subjected to different surface roughness excitations, noticeable vertical air gap eccentricity will occur.

This section first establishes a random road excitation displacement model based on the white noise model from the literature [26], as shown in Figure 16a. Subsequently, a vertical dynamics model of the hub motor is developed following the approach described in [27]. This leads to the vertical air gap eccentricity analysis under different road excitations, as Figure 16b depicts. Finally, the vertical air gap eccentricity is combined with the unbalanced radial force model proposed in Section 3 to obtain the unbalanced radial force plots for various road grades, as illustrated in Figure 16c.
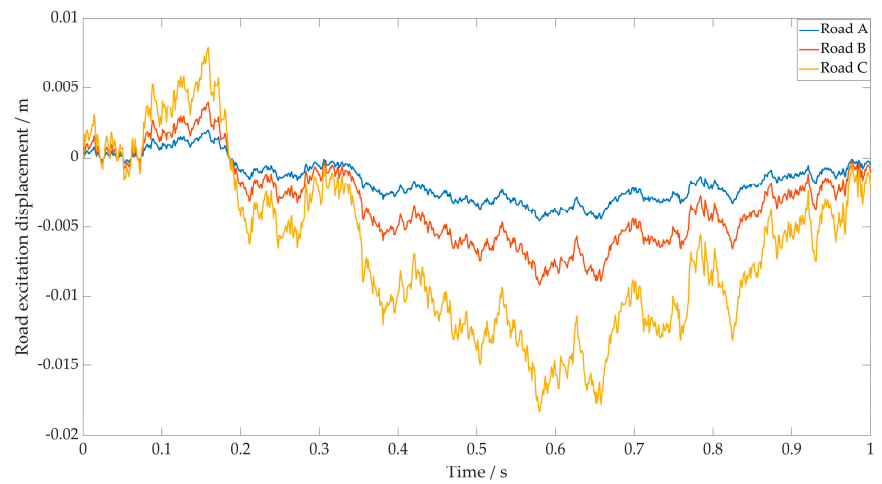
(**a**)
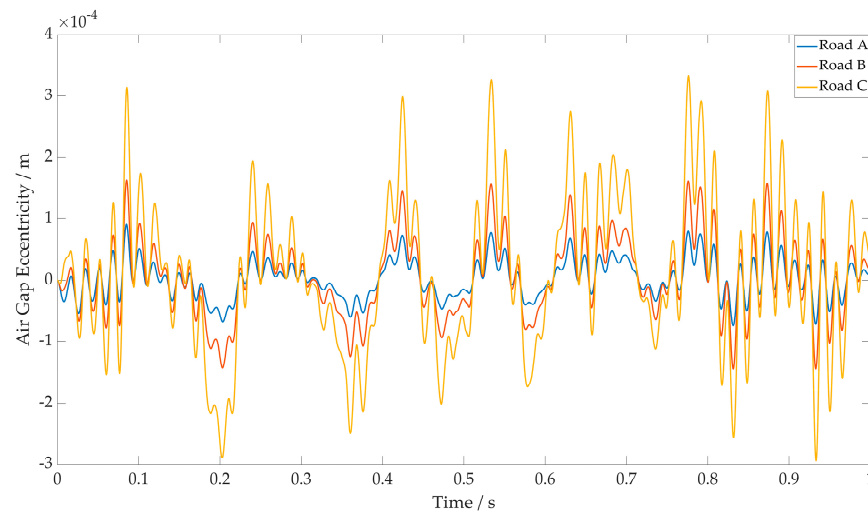
(**b**)
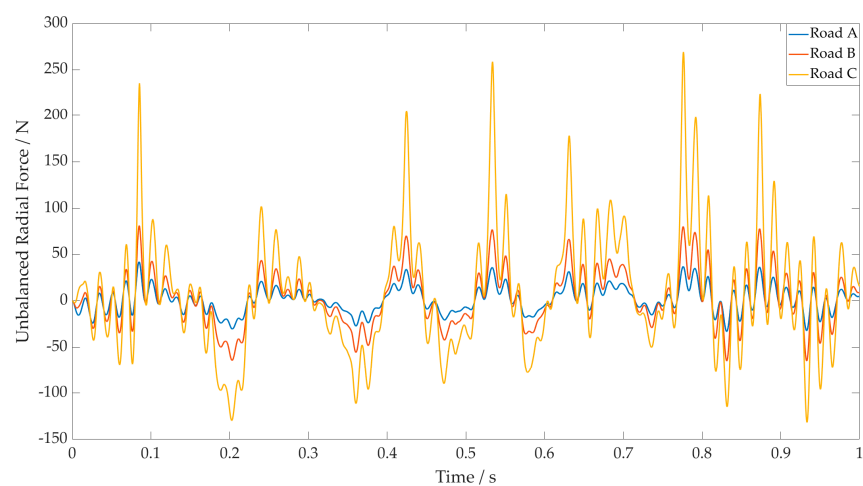
(**c**)

Figure 16. Change of air gap eccentricity length and unbalanced radial force under three kinds of road excitation. (**a**) Road excitation displacement z_g under different road ranks; (**b**) air gap eccentricity displacement under different road excitations; (**c**) unbalanced radial force under different road excitations.

Figure 16a indicates that as the road grade improves, the road unevenness gradually worsens, increasing the amplitude of road excitation displacement. Figure 16b shows that with the increasing amplitude of road excitation displacement, the vertical air gap eccentricity of the motor also increases, which further results in the increase of unbalanced radial force depicted in Figure 16c. This unbalanced radial force, induced by road excitation, can cause vibrations and noise in the motor, significantly affecting its operational quality.

When the switched reluctance hub-driven motor undergoes extreme steering, it is prone to tilt air gap eccentricity. This section focuses on the scenario of tilt eccentricity in the switched reluctance hub-driven motor during extreme steering conditions.

This section first derives the degree of tilt air gap eccentricity under extreme and large steering angles based on the switched reluctance hub motor steering model presented in reference [28], as shown in Figure 17a. Then, the obtained tilt air gap eccentricity curve is combined with the tilt eccentric unbalanced radial torque model proposed in the third section. This results in the unbalanced radial torque graph for different steering angles, as Figure 17b depicts.
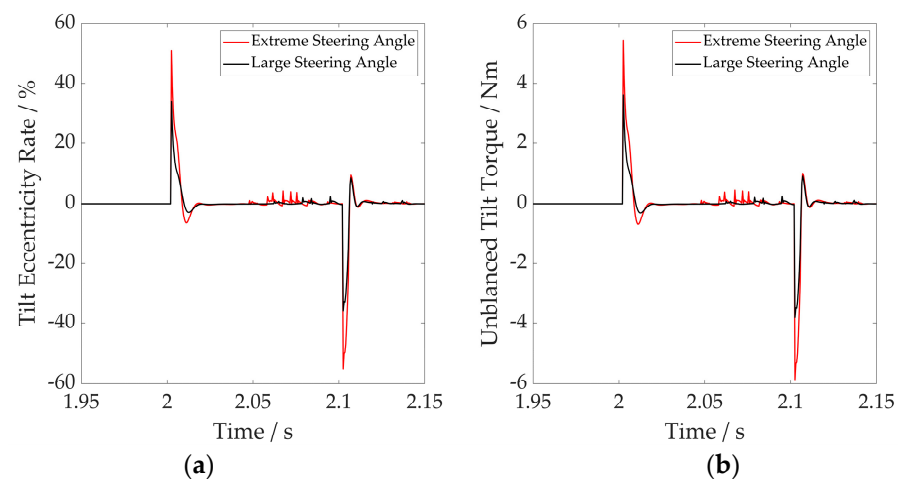

Figure 17. Tilt air gap eccentricity and unbalanced radial moment. (**a**) Tilt eccentricity under different rotation excitations; (**b**) unbalanced tilt torque under different rotation excitations.

Figure 17a shows that as the steering angle increases, the degree of tilt eccentricity at the start and end of the steering also increases. This phenomenon directly amplifies the unbalanced radial torque under tilt eccentricity, as Figure 17b shows.

These two typical scenarios illustrate that the type and extent of air gap eccentricity in the switched reluctance motor are directly influenced by external excitations, leading to electromagnetic force imbalance and resulting in unbalanced radial forces/torques.

5. Discussion

This paper improves the traditional calculation methods for radial electromagnetic force under vertical eccentricity, analyzing the geometric relationships of tilt eccentric air gap lengths. Combining these analyses, the expressions for radial electromagnetic force under tilt eccentricity and their distribution along the axial position are derived.

Using finite element software to model the radial force under vertical eccentricity, this paper directly obtains inductance data for various rotor angles, winding currents, and vertical air gap eccentricities. These data are then applied in commonly used methods, specifically the electromechanical conversion equations and the principle of virtual work, to derive a relatively accurate radial electromagnetic force under vertical eccentricity. Compared to traditional Fourier series fitting methods, this approach avoids the fitting errors that arise from limited sampling data.

Regarding modeling radial force under tilt eccentricity, this paper quantitatively analyzes the geometric relationships of air gap lengths under tilt eccentricity, resulting in

expressions for air gap lengths at different axial positions in the motor. Combining these tilt air gap length expressions with the expression for radial electromagnetic force under vertical eccentricity, the paper derives the expression for radial electromagnetic force under tilt eccentricity and its distribution curve along the axial direction. Experimental and finite element simulation results validate the accuracy of this method. Notably, this approach significantly reduces the complexity of analysis and computational load compared to the commonly used Maxwell stress tensor method while maintaining accuracy.

The authors also attempted to establish a dynamic simulation model for the switched reluctance motor to study the behavior of radial electromagnetic force under dynamic eccentricity. However, due to the oversight of the motor's mass during the testbench's construction, it was impossible to establish a dynamic motor test setup. Consequently, the authors could only rely on replicating experimental data from the literature for indirect validation, which was a necessary compromise.

In summary, the analytical model for radial electromagnetic force under air gap eccentricity proposed in this paper provides high accuracy and operability for analyzing the performance of radial forces under various eccentric conditions.

6. Conclusions

This paper discussed an analytical model for the radial electromagnetic force of switched reluctance motors under air gap eccentricity (vertical and tilt eccentricities). The model first derives the expression for radial electromagnetic force under different vertical air gap eccentricities. It then conducts a geometric analysis of the air gap length for the tilt air gap eccentricity, resulting in the distribution and expression of air gap length along the axial length of the motor for varying degrees of inclination. Finally, by combining the expressions for vertical eccentric radial electromagnetic force and the tilt eccentric air gap length, the expression for radial electromagnetic force under tilt eccentricity is obtained, along with its distribution along the axial length of the motor. Comparative experiments, simulations, and model results demonstrate that the proposed model accurately analyzes the behavior of radial electromagnetic force in switched reluctance motors under vertical and tilt eccentricities. Additionally, a dynamic model of the motor is established to analyze the behavior of air gap eccentricity and radial electromagnetic force in typical dynamic eccentric scenarios.

Author Contributions: Methodology, T.M.; Software, T.M.; Validation, Z.D. and W.L.; Data curation, M.H.; Writing—original draft, T.M.; Writing—review & editing, M.H.; Supervision, Z.D. and W.L.; Funding acquisition, Z.D. All authors have read and agreed to the published version of the manuscript.

Data Availability Statement: The original contributions presented in the study are included in the article, further inquiries can be directed to the corresponding author.

Conflicts of Interest: The author Wanli Liu was employed by the company China Merchants Testing Vehicle Technology Research Institute Co., Ltd. The author Zhaoxue Deng was employed by the company Changan Automobile Company Ltd. The remaining authors declare that the research was conducted in the absence of any commercial or financial relationships that could be construed as a potential conflict of interest.

References

1. Yan, W.; Chen, H.; Liu, Y.; Cheng, H.; Orabi, M. A Magnetic Field Decoupling Double Stator Switched Reluctance Machine. *IEEE Trans. Appl. Supercond.* **2021**, *31*, 1–5. [CrossRef]
2. Murty, V.S.; Jain, S.; Ojha, A. Analyzing modeled configuration using finite element analysis for performance prediction of LSRM. *Neural Comput. Appl.* **2022**, *34*, 21175–21189. [CrossRef]
3. Racha, A.; Guillaume, P.; Mounaim, T.; Jean-Philippe, L. Comparison of 8/6 radial and axial flux switched reluctance machines. *COMPEL* **2019**, *38*, 1756–1769.

4. Liang, W.; Wang, J.; Luk, P.C.K.; Fei, W. Analytical study of stator tooth modulation on the electromagnetic radial force in permanent magnet synchronous machines. *IEEE Trans. Ind. Electron.* **2020**, *68*, 11731–11739. [CrossRef]

5. Wang, F.; Wu, Z.; Li, X. Analytical modeling of radial coupled vibration and super-harmonic resonance in switched reluctance motor. *J. Vib. Eng. Technol.* **2021**, *9*, 449–467. [CrossRef]

6. Xu, M.-X.; He, Y.-L.; Zhang, W.; Dai, D.-R.; Liu, X.-A.; Zheng, W.-J.; Wan, S.-T.; Gerada, D.; Shi, S.-Z. Impact of Radial Air-Gap Eccentricity on Stator End Winding Vibration Characteristics in DFIG. *Energies* **2022**, *15*, 6426. [CrossRef]

7. He, Y.L.; Sun, Y.X.; Xu, M.; Wang, X.; Wu, Y.; Vakil, G.; Gerada, D.; Gerada, C. Rotor UMP characteristics and vibration properties in synchronous generator due to 3D static airgap eccentricity faults. *IET Electr. Power Appl.* **2020**, *14*, 961–971. [CrossRef]

8. Yavuz, S.; Parspour, N.; Ma, L. Analytical Modelling of a Parametrized Switched Reluctance Motor with Adapting Flux Tube Method. In Proceedings of the 19th IEEE International Conference on Industrial Technology (ICIT), Lyon, France, 20–22 February 2018.

9. Kondelaji, M.A.J.; Mirsalim, M. Non-linear Modeling of a Multi-Layer Switched Reluctance Motor with Magnetically-Disconnected Stator Modules. In Proceedings of the 10th International Power Electronics, Drive Systems and Technologies Conference (PEDSTC), Shiraz, Iran, 12–14 February 2019.

10. Ali, G.; Mojtaba, M. Split-Tooth Double-Rotor Permanent Magnet Switched Reluctance Motor. *IEEE Trans. Transp. Electrif.* **2022**, *8*, 2400–2411.

11. Mohammad Amin Jalali, K.; Ehsan Farmahini, F.; Mojtaba, M. Teethed-Pole Switched Reluctance Motors Assisted with Permanent Magnets: Analysis and Evaluation. *IEEE Trans. Energy Convers.* **2021**, *36*, 2131–2140. [CrossRef]

12. Roy, D.; Sengupta, M. An Experimentally Validated Novel Analytical Approach for Modeling of a Saturated Switched Reluctance Motor. *IEEE Trans. Magn.* **2022**, *58*, 1–11. [CrossRef]

13. Kadi, L.; Brouri, A.; Ouannou, A.; Lahdachi, K. Modeling and Determination of Switched Reluctance Machine Nonlinearity. In Proceedings of the 4th IEEE Conference on Control Technology and Applications (CCTA), Montreal, QC, Canada, 24–26 August 2020.

14. Sun, X.D.; Tang, X.T.; Tian, X.; Wu, J.L.; Zhu, J.G. Position Sensor-less Control of Switched Reluctance Motor Drives Based on a New Sliding Mode Observer Using Fourier Flux Linkage Model. *IEEE Trans. Energy Convers.* **2022**, *37*, 978–988. [CrossRef]

15. Chen, H.; Yan, W.J.; Chen, L.; Sun, M.; Liu, Z. Analytical Polynomial Models of Nonlinear Magnetic Flux Linkage for SRM. *IEEE Trans. Appl. Supercond.* **2018**, *28*, 5205307. [CrossRef]

16. Rocca, R.; De Donato, G.; Bolognesi, P.; Boccaletti, C.; Capponi, F.G. Improved Design-Oriented Analytical Modelling of Switched Reluctance Machines Based on Fröhlich-Kennelly Equations. *IEEE Trans. Energy Convers.* **2024**, *39*, 739–746. [CrossRef]

17. Zuo, S.; Liu, Z.; Hu, S. Influence of Rotor Eccentricity on Radial Electromagnetic Force Characteristics in Switched Reluctance Motors and Compensation. *Electr. Power Compon. Syst.* **2020**, *48*, 388–398. [CrossRef]

18. Hao, Y.; Wang, X.L.; Cui, R.Z.; Fang, X.Y.; Zhang, W.; Li, Y.H.; Cheng, D. Torque analytical model of switched reluctance motor considering magnetic saturation. *IET Electr. Power Appl.* **2020**, *14*, 1148–1153. [CrossRef]

19. Deng, Z.X.; Luo, X.L.; Liao, X.; Li, X.; Du, Z.; Hou, M.; Wei, H. Analysis and suppression of the negative effect of electromagnetic characteristics of wheel hub motor drive system on vehicle dynamics performance. In *Nonlinear Dynamics*; Springer: Berlin/Heidelberg, Germany, 2024. [CrossRef]

20. Farahani, E.F.; Kondelaji, M.A.J.; Mirsalim, M. An Innovative Hybrid-Excited Multi-Tooth Switched Reluctance Motor for Torque Enhancement. *IEEE Trans. Ind. Electron.* **2021**, *68*, 982–992. [CrossRef]

21. Hu, Y.H.; Deng, Y.; Liu, Q.W.; He, X.N. Asymmetry Three-Level Gird-Connected Current Hysteresis Control With Varying Bus Voltage and Virtual Oversample Method. *IEEE Trans. Power Electron.* **2014**, *26*, 3214–3222. [CrossRef]

22. Penovi, E.; Maestri, S.; Retegui, R.G.; Wassinger, N.; Benedetti, M. Control System for a Pulsed Current Source based on Digital Hysteresis and Current Estimation. *IEEE Lat. Am. Trans.* **2014**, *12*, 1214–1220. [CrossRef]

23. Ogbuka, C.; Nwosu, C.; Agu, M. A high performance hysteresis current control of a permanent magnet synchronous motor drive. *Turk. J. Electr. Eng. Comput. Sci.* **2017**, *25*, 1–14. [CrossRef]

24. Cho, H.J.; Kwon, Y.C.; Sul, S.K. Torque Ripple-Minimizing Control of IPMSM with Optimized Current Trajectory. *IEEE Trans. Ind. Appl.* **2021**, *57*, 3852–3862. [CrossRef]

25. Song, S.J.; Fang, G.L.; Hei, R.; Jiang, J.; Ma, R.; Liu, W. Torque Ripple and Efficiency Online Optimization of Switched Reluctance Machine Based on Torque per Ampere Characteristics. *IEEE Trans. Power Electron.* **2020**, *35*, 9608–9616. [CrossRef]

26. Shi, K.; Cheng, D.; Yuan, X.F.; Liu, L.; Wu, L. Interacting multiple model-based adaptive control system for stable steering of distributed driver electric vehicle under various road excitations. *ISA Trans.* **2020**, *103*, 37–51. [CrossRef] [PubMed]

27. Li, X.; Deng, Z.X. Negative dynamics effect of in-wheel switched reluctance motor with inclined airgap eccentricity on handing stability for electric vehicle. *Proc. Inst. Mech. Eng. Part D-J. Automob. Eng.* **2023**, *238*, 09544070231186198. [CrossRef]

28. Deng, Z.X.; Qin, H.S.; Ma, T.J. Negative effect and optimal control of in-wheel motor with inclined eccentricity on driving safety for electric vehicle. *Proc. Inst. Mech. Eng. Part K-J. Multi-Body Dyn.* **2024**, *238*, 14644193241260975. [CrossRef]